Earthquake Engineering & Structural Dynamics

WILEY

RESEARCH ARTICLE OPEN ACCESS

Energy-Based Characterisation of Earthquake Damage in Masonry Infills Through Combined In-Plane and Out-of-Plane Experimental Tests

Roberto Gentile[1] | Giulia Angelucci[2] | Jingren Wu[1] | Marilisa Di Benedetto[3] | Riccardo Milanesi[4] | Giulio Augusto Tropea[5] | Fabrizio Mollaioli[2] | Fatemeh Jalayer[1] | Fabio Freddi[6] | Fabio Di Trapani[7] | Paolo Morandi[4] | Gerard J. O'Reilly[8]

[1]Department of Risk and Disaster Reduction, University College London, London, UK | [2]Department of Structural and Geotechnical Engineering, Sapienza University of Rome, Rome, Italy | [3]Dipartimento Di Ingegneria Strutturale, Edile e Geotecnica, Politecnico Di Torino, Torino, Italy | [4]European Centre for Training and Research in Earthquake Engineering, Eucentre, Pavia, Italy | [5]Department of History, Design and Restoration of Architecture, Sapienza University of Rome, Rome, Italy | [6]Department of Civil, Environmental and Geomatic Engineering, University College London, London, UK | [7]Department of Engineering, University of Palermo, Palermo, Italy | [8]Centre For Training and Research on Reduction of Seismic Risk, Scuola Universitaria Superiore IUSS Pavia, Pavia, Italy

Correspondence: Roberto Gentile (r.gentile@ucl.ac.uk)

Received: 22 December 2025 | **Revised:** 21 April 2026 | **Accepted:** 19 June 2026

ABSTRACT

The seismic capacity of structural systems/members is usually defined in terms of deformation thresholds. Although this is effective in many circumstances, disregarding cumulative quantities such as hysteretic energy may be ineffective when low-cycle fatigue is relevant (e.g., long-duration ground motions, very soft soils, ground-motion sequences). This paper presents the outcomes of an experimental campaign designed to explore the suitability of hysteretic energy thresholds to characterise damage. To do so, three nominally identical masonry infill panels were subjected to in-plane (IP), quasi-static, cyclic displacement-controlled loads generating a moderate level of damage, followed by out-of-plane (OOP), dynamic shaking-table tests amplified until collapse. The study investigated the effect of the IP hysteretic energy dissipation on the observed IP damage state, and the subsequent OOP collapse capacity. Different IP loading protocols were designed to induce the same peak amplitude-based engineering demand parameters (EDPs) while modulating the energy-based demands. In the IP phase, two specimens showed a damage pattern dominated by sliding along two to three horizontal cracks, while the third specimen was dominated by a diagonal, strut-like failure. For the sliding-dominated specimens, the IP hysteretic energy showed signs of a positive correlation with the level of damage, and, in turn, a possible negative correlation with the peak floor acceleration leading to complete OOP collapse. On the one hand, further complementary experimental tests and/or refined numerical analyses are needed to generalise the trend highlighted here. On the other hand, the presented results pave the way for using energy-based EDPs for state-dependent seismic fragility assessment methodologies, thus allowing a refined consideration of damage accumulation.

1 | Introduction

Fragility functions play a crucial role in seismic risk assessment, enabling prioritisation of retrofitting efforts, the development of more effective building codes, and the allocation of resources for disaster preparedness and response. Fragility functions describe the probability of different assets reaching or exceeding different damage states (DSs) conditioned on one or more earthquake intensity measures (IMs). DSs are usually represented by thresholds of engineering demand parameters (EDPs), often expressed as peak response quantities such as displacements, drifts, or accelerations (i.e., ground or floor accelerations) over the duration of the ground shaking. Monotonic or quasi-static cyclic testing can provide such deformation thresholds for a given structural system or component, thus providing capacity limits to be checked against for different ground motions. Although such an approach implies a compromise in measuring dynamic response, it is economically ideal for estimating DSs since such tests do not depend on a specific ground-motion excitation input (thus not requiring several tests).

Recent research (e.g., [1, 2]) has investigated state-dependent fragility relationships beneficial for structures subjected to ground motion sequences (e.g., mainshock-aftershock). Most studies use the peak inter-storey drift as the measure of damage, although some models also take residual drift into account [3]. Peak or residual quantities, however, cannot adequately capture damage accumulation since they do not always monotonically increase with ground-motion intensity. Moreover, using these EDPs for state-dependent fragility analysis can lead to statistical inconsistencies. For example, a structure subjected to a given peak deformation (e.g., drift) will sustain a certain level of damage. If the structure is subjected to subsequent ground motions inducing similar or lower deformation levels, the damage level of the structure is expected to worsen to a lower or greater extent. However, if damage is measured with peak deformation-based DS thresholds, the structure will not be assigned a higher DS, but will remain in the same DS, thus providing a physically inconsistent characterisation of the structure's actual condition.

Integral-based quantities, such as hysteretic energy (E_h) or energy-based indices (e.g., [4–8]) can remedy the above inconsistency since they monotonically increase with the ground-motion excitation (or sequence) length, that is, they are cumulative. Several studies explicitly included cumulative EDPs in the design/assessment process [9–14]. A recent study by Gentile and Galasso [15] provides a hysteretic energy-based framework for state-dependent fragility development. The framework takes advantage of the demonstrated pseudo-parabolic relationship between the peak global deformation (e.g., maximum inter-storey drift) and the hysteretic energy of a system [16]. By characterising the median of this relationship via numerical analyses, it is possible to convert deformation-based damage thresholds into energy-based ones and characterise state-dependent fragility functions. Although the framework is theoretically sound, an experimental validation is still missing. On the other hand, Tropea et al. [17, 18] provide an analytical framework to characterise DSs directly using hysteretic energy and hysteretic power. The approach defines two ad hoc, energy-based indices and provides guidance to identify their thresholds for different DSs.

The ERIES-ENFRAG project (ENhancing state-dependent FRAGility through experimentally validated Energy-Based Approaches), presented in this paper, provides an experimental campaign specifically tailored to aid the validation of hysteretic energy-based fragility assessment approaches, which are: (1) currently based only on analytical and/or numerical validations; (2) only considering one type of action/damage mechanism. Masonry infill panels are a suitable candidate to address the research question because they are normally subjected to a combination of in-plane (IP) and out-of-plane (OOP) loads, as well as being particularly common in many building classes (especially in Europe). Therefore, the ENFRAG project focuses on masonry infill panels experiencing cumulative states of damage due to combinations of IP quasi-static cyclic and OOP dynamic actions. Among several experimental setups adopted for IP and/or OOP tests on masonry infills (e.g., [19–24]), ENFRAG exploits and builds upon previous results obtained by Morandi et al. [25] since it involves a sequential IP/OOP protocol fully consistent with the aims of this study and provides a solid basis for calibrating the loading protocols adopted herein.

The paper is structured as follows: Section 2 describes the rationale of the experimental campaign, the test specimens and loading protocols, and the related numerical studies for the calibration of such loading protocols; Section 3 provides a detailed description of the test results, together with their interpretation; Section 4 shows how the interpretations can contribute to validate the hysteretic energy-based fragility approach, as well as identify further investigations required to complete such validation.

2 | Experimental Campaign

2.1 | Rationale

The ENFRAG experimental campaign involved three nominally identical full-scale masonry panels (denoted SP1, SP2, SP3) subjected to: (1) quasi-static, cyclic IP loads achieving a selected drift level; (2) subsequent OOP shaking table testing in which a selected motion was sequentially applied, increasing its amplitude, until complete collapse. The experimental campaign was designed to study the effect of IP hysteretic energy on the induced IP DS and, subsequently, on the OOP capacity. This was obtained by subjecting the specimens to the same values of IP peak-based EDPs while modulating the energy-based demand conditional on the above peak quantities ($E_h|EDP_{IP}$). Similar OOP load protocols were then applied to all specimens.

To increase the available data without increasing the cost of the experimental campaign, ERIES-ENFRAG strategically leverages the results of the experimental campaign by Morandi et al. [25], which adopts the same test setup and four masonry infill specimens that were nominally identical to those considered herein. The only differences in the considered specimens relate to the construction time of the infills and the production batches of clay units and mortar. Therefore, the main differences among the current and the reference tests are the IP and OOP load protocols. The IP results of two reference tests were used to characterise the median $E_h|EDP_{IP}$ of the specimens and calibrate a numerical model accordingly. A parametric analysis of this model allowed modulating the adopted IP load protocols and controlling the $E_h|EDP_{IP}$ imparted to the specimens. The following subsections provide extensive details on the specimens, the test setup, the adopted loading protocols, the procedure used to calibrate them, and the criteria adopted to identify different DSs in the tests.

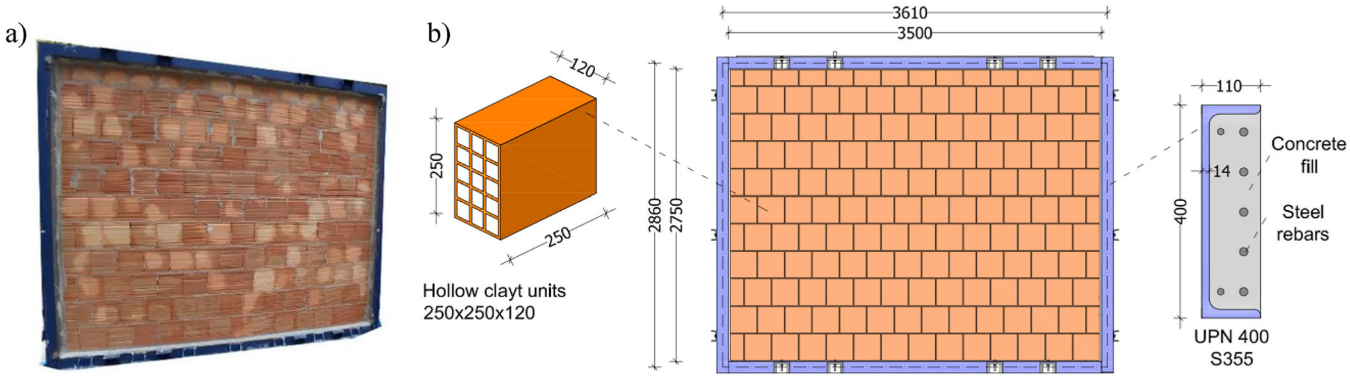

FIGURE 1 | Details of the considered specimens: (a) View of a specimen; (b) Geometric details. [Dimensions in mm].

2.2 | Description of the Specimens

The three masonry panels were 3.50 m wide, 2.75 m tall, and 13 cm thick (including 1 cm of plaster on one side). The infills were constructed within a rectangular structural frame with steel-concrete composite sections made of UPN400 steel elements (steel grade S355) grouted with high-strength concrete with steel reinforcement (Figure 1). The elastic lateral stiffness of the frame is equal to 1.644 kN/mm. Consistent with the tests by Morandi et al. [25], the frame was designed to mimic the IP deformation of a non-seismically designed RC frame, whilst remaining nearly elastic during the tests. This practical choice allowed the continued re-use of the composite frame. Morandi et al. [25] conducted preliminary cyclic tests on the bare frames to pre-crack the concrete in the composite sections of the frame elements, ensuring that each frame had a similar level of damage and stiffness before the infilled tests. By doing so, the composite frame could mimic the behaviour of an RC frame, especially for frames with weak masonry, for which the local interaction effects on the bounding frame with the infills are limited. Consistently, the tested infill typology involved a single layer of 12 cm thick, horizontally hollowed clay units (nominal dimensions: 12 × 25 × 25 cm, nominal volumetric percentage of holes: 65 %). To mimic the typical construction typology in Italy in the 1960s–1980s, a general-purpose mortar type denoted M2.5 was used, which had a nominal compression strength equal to 2.5 MPa. Mortar beds were 1 cm thick, and the mortar head-joints were loosely filled to resemble the Italian construction techniques of the 1960s–1980s. To achieve full adherence with the structural frame, the interface joint at the edges was filled with mortar.

2.3 | Materials Characterization Tests

Material tests were conducted to characterise the relevant properties, which are summarised in Table 1. The clay units were tested according to EN 772–1 [26] to evaluate their compressive strength units under vertical (i.e., perpendicular to holes, f_b) and lateral compression (i.e., parallel to holes, f_b'). The flexural (f_{fl}) and compressive strength (f_m) of the mortar were characterised according to EN 1015–11 [27]. Moreover, masonry wallets composed of 3 × 3 clay units (i.e., 77 × 77 cm) were tested in compression according to EN 1052–1 [28] to evaluate their compressive strength and elastic moduli, both in the vertical (i.e., perpendicular to holes, f_{vert}, E_{vert}) and horizontal (i.e., parallel to holes, f_{hor}, E_{hor}) directions, and separately considering different units with and without plaster. The elastic moduli were evaluated from the stress-strain curve slopes at one-third of the wallets' peak strength. The diagonal tensile strength (f_t) and the shear modulus (G) of the masonry were characterised with diagonal compression tests consistent with ASTM E519-02 [29] and carried out on 129 × 129 cm masonry specimens. The OOP flexural strength of the masonry was evaluated according to EN 1052–2 [30] using 129 × 51 cm specimens for the vertical direction (i.e., parallel to the bed-joints, f_{x1}). Three specimens were tested by applying the load from the plastered side (i.e., plaster in compression), and three more from the side without plaster (i.e., plaster in tension). The initial shear strength (f_{v0}) and the friction coefficient (μ) of the bed joints were tested on "triplets" made of three clay units according to EN 1052–3 [31]. Those were tested in the direction parallel to the bed joints, and for three levels of horizontal compression f_p (i.e., 0.1, 0.2, and 0.3 MPa).

2.4 | Test Setup and Instrumentation

Figure 2a illustrates the experimental setup used for both IP and OOP tests [25]. The specimen was fixed to a 4.80 × 4.80m, 6DOF shaking table [32], which acted as a strong floor during the IP tests. The connection was made through a 4.25m-long steel foundation beam composed of two HEB400 beams welded together and stiffened with 10mm-thick vertical plates. Thirty-four M30 bars connected the foundation beam to the shaking table, while 14 more connected the foundation beam with the composite frame. A steel beam was also connected to the top of the composite frame through 28 M18 and 4 M27 bolts to stiffen the upper part of the frame. This was made with a HEA200 profile equipped with two steel girder boxes restrained at the top corners of the frame. The boxes allow the frame to be connected to the shake table through four diagonal bracings constituted by steel square tubular profiles. Class S355 steel was adopted for all steel members. The diagonal connections provided OOP restraint of the frame, thus avoiding any unintended OOP deformation in the IP phase of the tests and allowing only the acceleration/displacements of the infill relative to the frame in the OOP phase of the tests. A servo-hydraulic actuator (500 kN maximum capacity) connected one of the steel boxes to a strong steel structure, acting as a strong wall, and allowing the application of the load in the IP phase of the tests.

TABLE 1 | Mechanical properties of the materials.

Material	Property	Symbol	Mean	CoV	N specimens	Test standard
Clay units	Vertical compressive strength	f_b	7.20 MPa	14.10%	10	EN 772-1
	Horizontal compressive strength	f'_b	4.04 MPa	14.50%	10	EN 772-1
Mortar	Flexural strength	f_{fl}	0.384 MPa	20.30%	11	EN 1015-11
	Compressive strength	f_m	1.553 MPa	13.80%	24	EN 1015-11
Masonry	Vertical compressive strength	f_{vert}	1.503 MPa	17.80%	3	EN 1052-1
	Vertical elastic modulus	E_{vert}	3811 MPa	17.00%	3	EN 1052-1
	Horizontal compressive strength	f_{lat}	2.557 MPa	7.50%	3	EN 1052-1
	Horizontal elastic modulus	E_{lat}	2683 MPa	41.50%	3	EN 1052-1
	Diagonal tensile strength[a]	f_t	0.156 MPa	11.70%	3	ASTM E519
	Shear modulus	G	1451 MPa	14.50%	3	ASTM E519
	Vertical flexural strength (plastered side in tension)	f_{x1}	0.390 MPa	23.80%	3	EN 1052-2
	Vertical flexural strength (plastered side in compression)	f_{x1}	0.302 MPa	9.90%	3	EN 1052-2
	Density	ρ	1034 kg/m^3	1.90%	6	
Bed joints	Initial shear strength	f_{v0}	0.206 MPa	—	9	EN 1052–3
	Friction coefficient	μ	0.583	—	9	EN 1052–3

[a]The diagonal tensile strength was computed as $f_t = F_{max}/[t\times(l_1+l_2)]$, where F_{max} is the force at failure, t is the thickness, l_1 and l_2 are the height and length of the specimen.

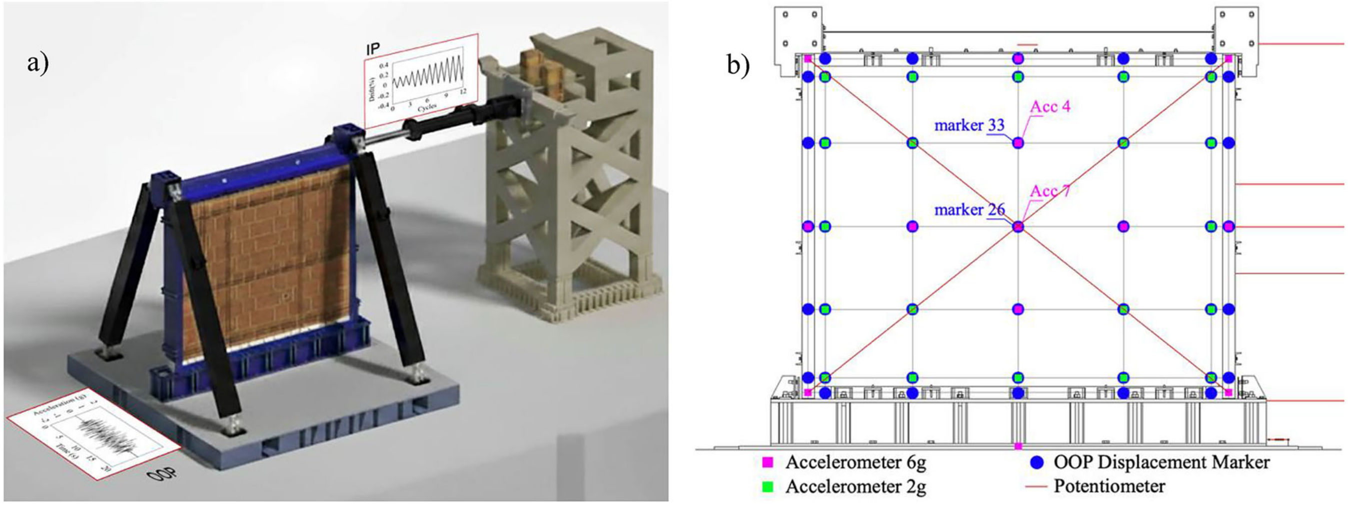

FIGURE 2 | (a) Sketch of the experimental setup adopted for the cyclic in-plane and dynamic out-of-plane tests. (b) Location of the installed accelerometers and markers for displacement measurement.

This configuration allowed the test setup to be changed for the IP and OOP phases without moving the test specimen. In the IP phase, the loads were applied in displacement control through the actuator, while an active control allowed the shake table to remain stationary, therefore acting as a strong floor. Prior to the OOP test, the setup was changed by removing the actuator while keeping the diagonal restraints. The OOP motions were directly exerted on the shaking table.

The measuring instrumentation differed in the two phases. Linear transducers were adopted in the IP phase. Such instruments allowed measuring the distribution of displacements and drifts of the specimen. Additionally, accelerometers were installed to monitor the evolution of the OOP fundamental frequency, measured via an impulsive excitation (i.e., hammer test). These were applied after each IP test phase, including IP cycles at the same target. Accelerometers with different sensitivities (i.e., 2 and 6 g) were used for the different parts of the masonry wall. In addition to the above, the OOP phase included an optical acquisition with markers and high-resolution infrared cameras used to measure OOP displacements according to the distribution displayed in Figure 2b.

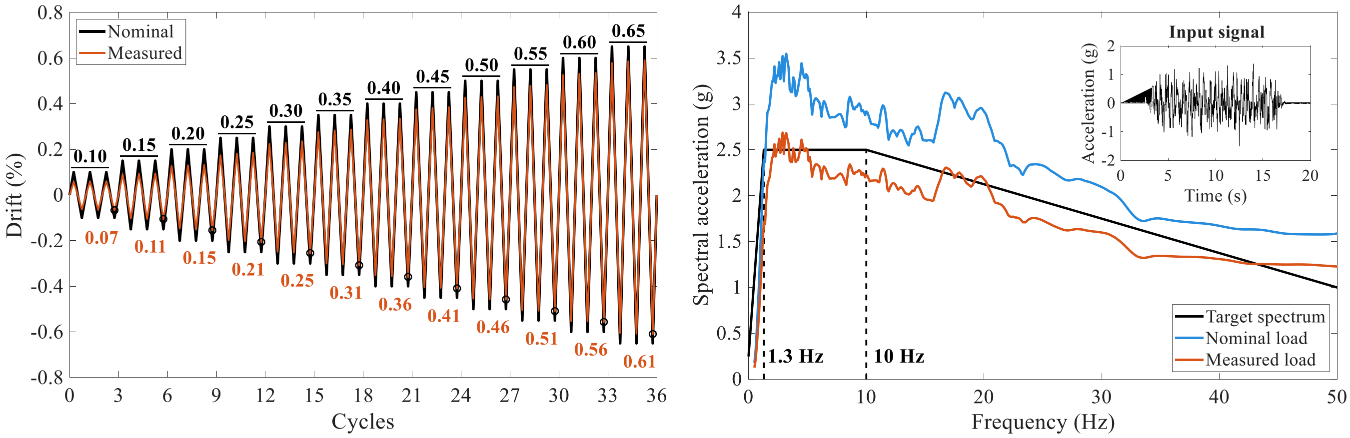

FIGURE 3 | Example loading protocols (SP3): (a) in-plane; (b) out-of-plane.

TABLE 2 | Test programme.

	Nominal in-plane drift levels (%)	c	Nominal out-of-plane PFA levels (g)	Notes
Ref1	0.10, 0.20, 0.30, 0.40, 0.50, 0.65	3	0.10, 0.20, 0.30, 0.40, 0.50, 0.75, 1.00, 1.25, 1.50, 1.50	**Baseline** $E_h\|EDP_{IP}$ T3 in Morandi et al., 2025 [25]
Ref2	0.05, 0.10, 0.20, 0.30	3	0.10, 0.20, 0.30, 0.40, 0.50, 0.75, 1.00, 1.25, 1.50, 1.80, 2.00, 2.25, 2.50	Lighter IP damage T2 in Morandi et al., 2025 [25]
Ref3	0.10, 0.20, 0.30, 0.40, 0.50, 0.75, 1.00	3	—	Reference; only IP T1 in Morandi et al., 2025 [25]
SP1	0.10, 0.20, 0.30, 0.40, 0.50, 0.65	1	0.10, 0.20, 0.30, 0.40, 0.50, 0.75, 1.00, 1.25, 1.50, 1.75, 2.00, 2.25, 2.50, 2.50, 2.50	**Less** $E_h\|EDP_{IP}$ decreasing EDP_{IP} cycles
SP2	0.10, 0.20, 0.30, 0.40, 0.50, 0.65	6	0.10, 0.20, 0.30, 0.40, 0.50, 0.75, 1.00, 1.25	**More** $E_h\|EDP_{IP}$ increasing EDP_{IP} cycles
SP3	0.10, 0.15, 0.20, 0.25, 0.30, 0.35, 0.40, 0.45, 0.50, 0.55, 0.60, 0.65	3	0.10, 0.20, 0.30, 0.40, 0.50, 0.75, 1.00, 1.25, 1.50, 1.75	**More** $E_h\|EDP_{IP}$ increasing EDP_{IP} cycles

Abbreviations: c: number of cycles per IP drift level; PFA: peak floor acceleration.

2.5 | Loading Protocols

Figure 3 shows the sequential IP and OOP loading protocols adopted in the campaign (using SP3 as an example), while Table 2 summarizes their parameters for all the specimens, also considering analogous information from the reference tests reported by Morandi et al. [25]. The IP loading protocols involved executing displacement-controlled loading cycles at progressively higher drift levels, imposing d levels of horizontal drift $\theta_{max} = [\theta_1, \ldots, \theta_d]$, each involving full cycles $[0, \theta_{max}, -\theta_{max}, 0]$ repeated c times. Since no specific feedback loop was implemented during IP displacement application, the actual displacements recorded by the installed transducers ("measured load" in Figure 3a) were slightly different from target drift levels of the specific IP loading protocol ("nominal values" in the figure). The OOP loading protocol involved a series of shaking table motions with increased intensity until reaching the complete collapse of the infill. The baseline input signal was generated as an artificial motion matching a horizontal required response spectrum (RRS). Consistently with the guidelines in ICC ES AC156 [33], the spectrum exhibits a tri-linear functional form showing a plateau within the frequencies f_1 and f_2. Such frequencies were set to 1.3 and 10.0 Hz, respectively, to encompass the full range of natural frequencies of the infills, while the baseline peak floor acceleration (PFA) was set to 1 g. The baseline record was generated as a broadband random excitation with a 25-second duration, comprising a 5-second rise time, 15 s of sustained strong motion, and a 5-second decay phase, assuming a 5% damping ratio for all frequencies. For each OOP test run, the baseline motion was linearly scaled in amplitude to obtain a selected nominal value of PFA. The procedure was repeated, increasing the PFA until the specimen's OOP collapsed. Due to the transfer function of the shaking table, a slight discrepancy between the nominal and measured acceleration signals was observed. However, white noise tests performed before each OOP run, allowed the characterization of the specimen's dynamic properties and the tuning of the shaking table for the following test, thereby ensuring the match of the measured and target spectrum (see Figure 3b). These tests consisted of a low-level acceleration flat-spectrum signal with frequency content ranging from 0.50 to 50 Hz, with a duration of at least 180 s.

Specimens SP1, SP2, and SP3 were subjected to the same maximum IP nominal drift equal to 0.65%. This level of drift was set to produce moderate IP damage to the specimen, thereby enabling meaningful OOP tests. Such maximum drift was the same of specimen Ref1 (termed T3 in Morandi et al. [25]), which was used as a baseline for the IP hysteretic energy|drift relationship ($d = 7$ drift levels; $c = 3$ cycles per drift level). The IP protocol for SP1 was calibrated to obtain a lower-than-baseline hysteretic energy|drift relationship by reducing the number of cycles per drift ($d = 7$ drift levels, identical to Ref1; $c = 1$ cycle per drift level). The IP protocol of SP2 allowed a higher-than-baseline hysteretic energy|drift relationship to be obtained by increasing the number of cycles per drift ($d = 7$ drift levels; $c = 6$ cycle per drift level). The SP3 achieved the same hysteretic energy|drift relationship of SP2 through a higher number of drift levels but a lower number of cycles ($d = 12$ drift levels; $c = 3$ cycle per drift level). All specimens were subsequently subjected to the same OOP protocol as detailed above. The following Section 2.6 presents the preliminary numerical analysis conducted to calibrate the load protocol for each specimen, specifying the selected drift levels and the number of cycles applied.

2.6 | Numerical Calibration of the IP Test Protocols

The IP response of the infill walls was reproduced by adopting an equivalent-strut macro-model approach. The infill panel was simulated using two concentric, compression-only diagonal struts, with equivalent width determined following the relationship proposed by Smith [34]. A multi-linear horizontal force-displacement envelope was implemented in OpenSees using the *HystereticSM* uniaxial material [35]. The monotonic backbone curve was initially derived from mechanics-based relationships, according to the constitutive model of Liberatore et al. [36]. The response envelope was characterized by the un-cracked phase up to the infill's first cracking, the post-cracking phase up to the peak strength, and the post-peak strength deterioration up to collapse. A pushover analysis was performed on specimens Ref1, Ref2, and Ref3 as a preliminary "sanity check" and the results were compared with the experimental data of the reference campaign [25]. This allowed for a crucial refinement in the mechanics-based calibration: instead of using the theoretical peak strength of the initial backbone curve, the mean peak strength observed in the reference tests was used to better align the model with experimental observations. The force (F) and displacement (d) values for the IP monotonic backbone curve of the *HystereticSM* uniaxial material were defined as follows: $F = [136; 170, 60]$ kN and $d = [0.0013; 0.0066, 0.1142]$ m.

The hysteretic parameters for stiffness and strength degradation were calibrated using a maximum likelihood estimator and all the experimental data available from the reference tests (i.e., the quasi-static cyclic IP data related to specimens Ref1, Ref2, and Ref3) expressed in the form ${E_H}^{EXP,k}(\theta_{max,i})$. In this notation, k indicates the specimen and its IP load protocol (see Table 2), while $\theta_{max,i}$ indicates the absolute value of the maximum drift experienced by the specimen up to step i of the test (note that the test was monitored several times per each drift cycle). The macro-model was parameterised as a function of the parameters of the *HystereticSM* model in OpenSees, $H = [h_1, \ldots, h_5]$, and the push-pull load protocol of the reference experimental tests, $load_k$. The hysteretic energy calculated for such analyses is ${E_H}^{NUM,k}(\theta_{max,i}, H)$, where the superscript k indicates the loading protocol. This is obtained by direct integration of the force-displacement measurements, without discounting for the elastic energy (which becomes zero at the end of the test).

Consistently with Gardoni et al. [37], the likelihood of the macro model observing the test data ${E_H}^{EXP,k}(\theta_{max,i})$ is expressed by Equation (1), where σ is a parameter expressing model uncertainty, ${r_i}^k(H)$ represents a distance function between the experimental and numerical hysteretic energy (Equation 2), and φ is the standard Normal probability density function. Using a genetic algorithm optimisation [38], the likelihood denoted by Equation (1) was maximised to find the optimal vector of hysteretic parameters H^* needed for the *HystereticSM* model in OpenSees. To the best of the authors' knowledge, such a calibration has not been used before in the context of experimental tests.

$$L(H, \sigma) \propto \prod_{i,k} \frac{1}{\sigma \theta_{max,i}} \varphi \left[\frac{{r_i}^k(H)}{\sigma \theta_{max,i}} \right] \tag{1}$$

$${r_i}^k(H) = \left| {E_H}^{EXP,k}\left(\theta_{max,i}\right) - {E_H}^{NUM,k}\left(\theta_{max,i}, H\right) \right| \tag{2}$$

The calibrated parameters for the *HystereticSM* uniaxial material in OpenSees included: 0.817 and 0.112 as the pinching factors during reloading for deformation (*pinchx*) and force (*pinchy*), respectively; 0.0001 and 0.0077 for damage due to ductility (*damage1*) and energy (*damage2*), respectively; 0.499 as the power used to determine the degraded unloading stiffness based on ductility (*beta*). Figure 4a shows the calibration results, indicating a satisfactory match between the numerical and experimental results of the hysteretic force-displacement response. Moreover, Figure 4b shows that the computed hysteretic energy lies between the two experimental datasets, which is the primary goal of the calibration. Using the calibrated macro-model of the infilled frame, a cloud analysis was subsequently carried out, adopting a set of 348 real (i.e., recorded) ground motions selected from the database introduced in Gutiérrez-Urzúa et al. [24], considering the following criteria: (1) non-pulse-like records; (2) strong ground motions (i.e., peak ground velocity > 0.3m/s). These analysis results were used to characterise the probability distribution of the dynamic hysteretic energy versus maximum deformation (i.e., $E_h|\theta_{max}$), as presented in Figure 5a (i.e., Cloud median and Cloud $\pm 1\sigma$). Finally, a parametric push-pull analysis of the optimised model was conducted by varying the IP load parameters (i.e., c, d), allowing a mapping between those parameters and the hysteretic energy to be established, as shown in Figure 5b. Based on this mapping, the IP load protocols of SP1, SP2, and SP3 were defined (as per Table 2) to modulate their $E_h|\theta_{max}$ response. Specimen SP1 targeted a hysteretic dissipation approximately one standard deviation below the mean $E_h|\theta_{max}$ dynamic response: this was obtained using the same drift amplitudes as in Ref1, but with one cycle per drift amplitude. Specimens SP2 and SP3 targeted a $E_h|\theta_{max}$ response one standard deviation above the dynamically computed mean. SP2 obtained it with the same drift

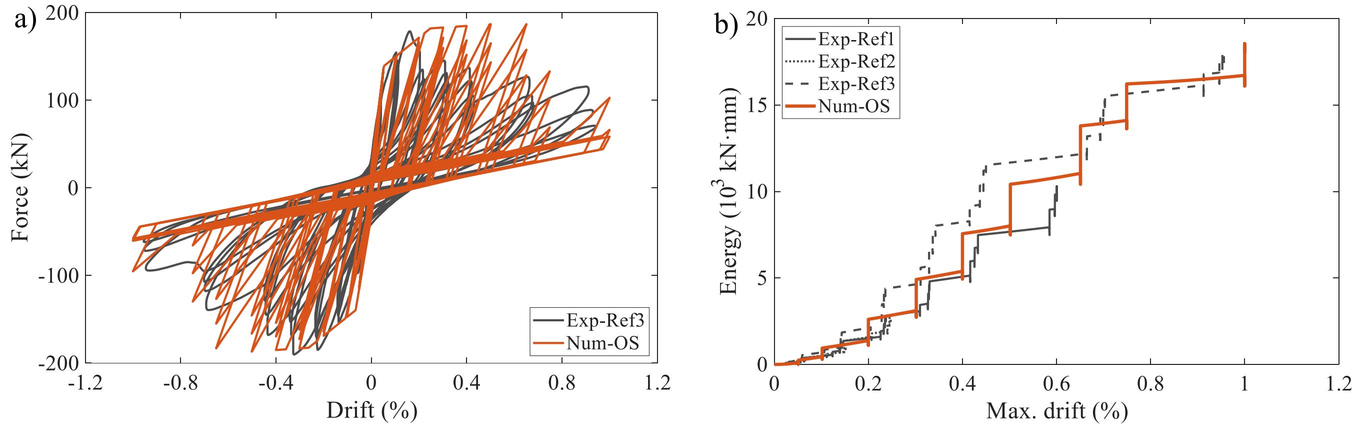

FIGURE 4 | Calibration of the macro-model in OpenSees against the reference experimental tests: (a) force-displacement; (b) energy-drift.

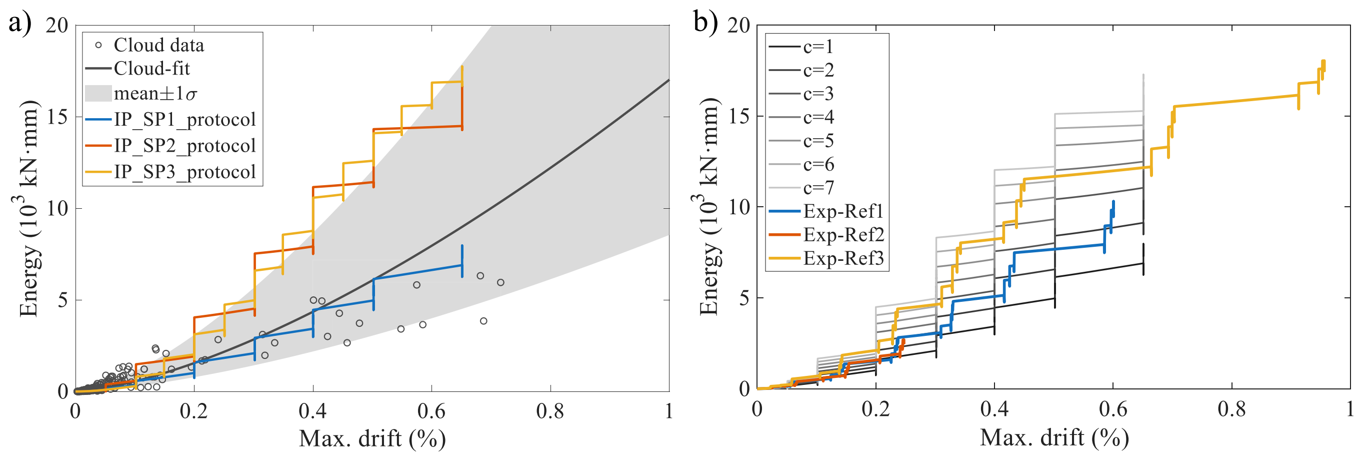

FIGURE 5 | (a) Parametric push-pull analysis on the calibrated macro-model; (b) Selected IP protocols for specimens SP1, SP2, and SP3.

amplitudes as in Ref1 but with six cycles per drift amplitude, while SP3 obtained it with a different set of amplitudes, each repeated three times.

2.7 | Adopted Criteria for DS Detection

The definition of DSs for masonry infills is conventionally based on the observation of the extent and severity of damage patterns from experimental tests and/or post-seismic reconnaissance missions. Typical DSs for IP actions correspond to: onset of cracking and initial detachment between the infill panel from the surrounding RC frame; widening of pre-existing damage patterns; crushing and spalling of a considerable number of brick units; partial or total collapse of the infill panel. This damage description often includes a quantitative indication of crack width, making it a useful tool for practitioners. For instance, it is frequently used in survey forms like AeDES (Usability and Damage in Post-Earthquake Emergency [39]) and can be easily correlated with the required repair efforts [40–42]. Additionally, such damage levels can be related to the attainment of characteristic points on the force-displacement backbone curve of the infilled frame (e.g., [40, 43]). Also, consistently with Eurocode [44], the point corresponding to the peak force usually defines a damage limitation DS, a fraction of its drift (typically between one- and two-thirds) defines the immediate occupancy DS, while a complete DS corresponds to a 40%-50% drop in force below the peak. Finally, drift/displacement thresholds for such DSs are available for developing fragility functions (e.g., [40–42, 45]).

In this study, three distinct IP DSs were defined by combining and synthesising the aforementioned phenomenological definitions, allowing for an objective and quantitative appraisal of the panel area extension affected by cracks and/or possible failure of brick units to be defined. DS0 (Cosmetic Damage) is defined corresponding to the detachment of the masonry panel from the perimeter frame, specifically at the intrados of the top beam and/or along the upper half-height of the columns. This DS corresponds to a negligible amount of energy dissipated via hysteresis. DS1 (Slight Damage) corresponds to light cracking, either in the bed- and head-joints or diagonally, or in the plaster. Isolated spalling of individual masonry units can also occur. At DS2 (Moderate Damage), the cracks developed at DS1 widen and propagate through both mortar joints and masonry units. Additionally, new diagonal cracks were expected to form in both directions, affecting approximately 30% of the panel area. This stage may also involve sliding between joints or localised crushing of units at the corners or centre of the infill, impacting about 10% of the panel. More severe IP DSs are not defined here, as they were not relevant for the present study.

TABLE 3 | Criteria to identify in-plane (IP) and out-of-plane (OOP) damage states (DSs).

	In plane	Out of plane
DS0 Cosmetic damage	Observe at least one among: 1. Detachment of the infill from the frame (at the intrados top beam) 2. Upper half-height of any column	Not observable in the OOP test phase
DS1 Slight damage	Observe at least one among: 1. Light cracks in masonry (bed- and head-joints or diagonal) 2. Light cracks in plaster 3. Spalling of single masonry unit	Not observable in the OOP test phase
DS2 Moderate damage	Observe at least one among: 1. Notable evidence of joint sliding 2. Bi-diagonal cracking (through 3. Localised (10%) crushing of any zone (corner or centre) 4. Significant (30%) area of the panel affected by cracks	Not observable in the OOP test phase
DS3 Extensive damage	Not observable in the IP test phase	Observe at least one among: 1. Distinct OOP detachment of the panel from the surrounding frame 2. Severe crushing and spalling of masonry units 3. Fall of individual masonry units and formation of openings accumulation
DS4 Collapse	Not observable in the IP test phase	Observe at least one among: 1. Out-of-plane expulsion of a large section of the infill 2. Total collapse of the infill panel

Table 3 provides the measurable criteria adopted in this study to identify the damage levels suffered by the infills during the experimental tests. Specific drift thresholds for each DS were identified through direct, qualitative damage observations after each analysed drift level in the IP phase, including a manual tracking of the cracking pattern. When a given DS was observed at the end of a specific drift level, it indicates that the corresponding damage occurred at some point during that drift increment. Because the same DS was not observed in the preceding IP phase, it was inferred that the DS was triggered within the drift range bounded by the maximum drift of the previous phase and that of the current phase. For example, in specimen SP1, DS2 was identified after the third analysed drift level, with 0.26% drift amplitude. Since DS2 was not observed after the second drift level (0.16%), it is inferred that DS2 was triggered between 0.16% and 0.26% drift (see Figure 6 in Section 3.1).

A similar approach was pursued for characterising OOP damage, although defining progressive and quantifiable OOP DSs posed greater challenges than for IP conditions. This was primarily attributed to the prevalence of sudden, brittle OOP collapse mechanisms, the intricate interaction with pre-existing IP damage, and the limited previous experimental literature. Most studies (e.g., [19, 46]) present experimental results detailing OOP damage evolution through characteristic points on the force-displacement response of the infills. However, a fully consolidated, universally accepted formalisation for OOP DSs remains to be established. An attempt was made by Furtado et al. [47], who categorised the observed damage in masonry infills subjected to pure OOP loadings into four DSs.

In the present work, the OOP DSs lower than the moderate damage are not defined, since the OOP tests start with pre-existing IP damage. DS3 (Severe Damage) is defined corresponding to widespread crushing and spalling of masonry units in previously damaged areas. This stage was marked by the critical weakening and imminent failure of the OOP arching mechanism. This can manifest as apparent OOP detachment of the panel from the surrounding frame, often coupled with intensified damage and crushing at the upper boundary. Alternatively, the falling of individual masonry units and the formation of openings within the panel may be observed, alongside extensive plaster detachment, pulverised mortar, and significant debris accumulation. DS4 (Collapse) corresponds to the condition where the infill has lost stability, culminating in partial or complete collapse mechanisms. This may include an evident horizontal flexural mechanism in the masonry portion above or below an opening, or the OOP expulsion of a large section of the infill. Table 3 provides the measurable criteria adopted in this study to identify the damage levels suffered by the infilled frames during the

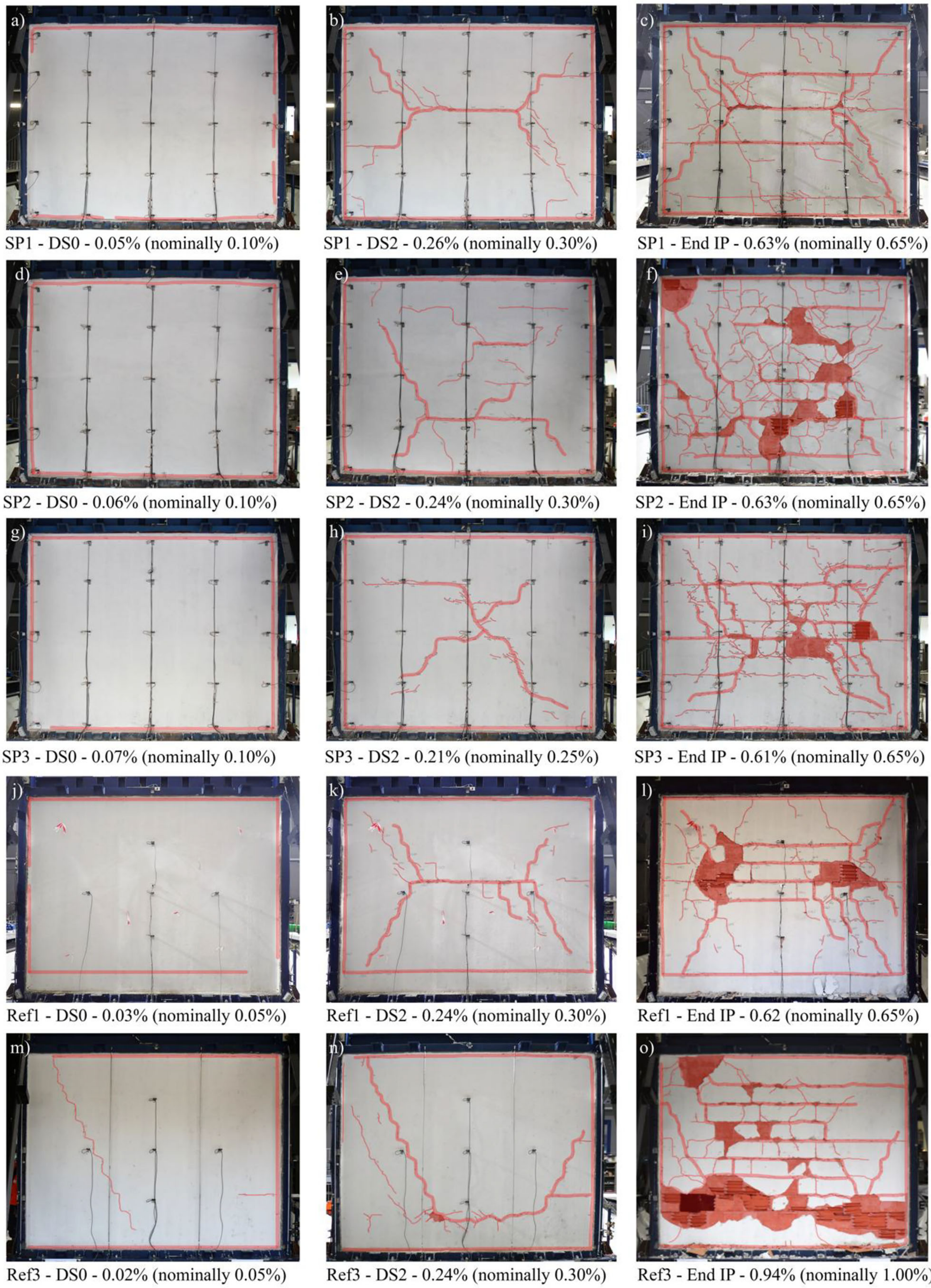

FIGURE 6 | Snapshots of the masonry infills at the attainment of DS0, DS2, and at the end of the in-plane test.

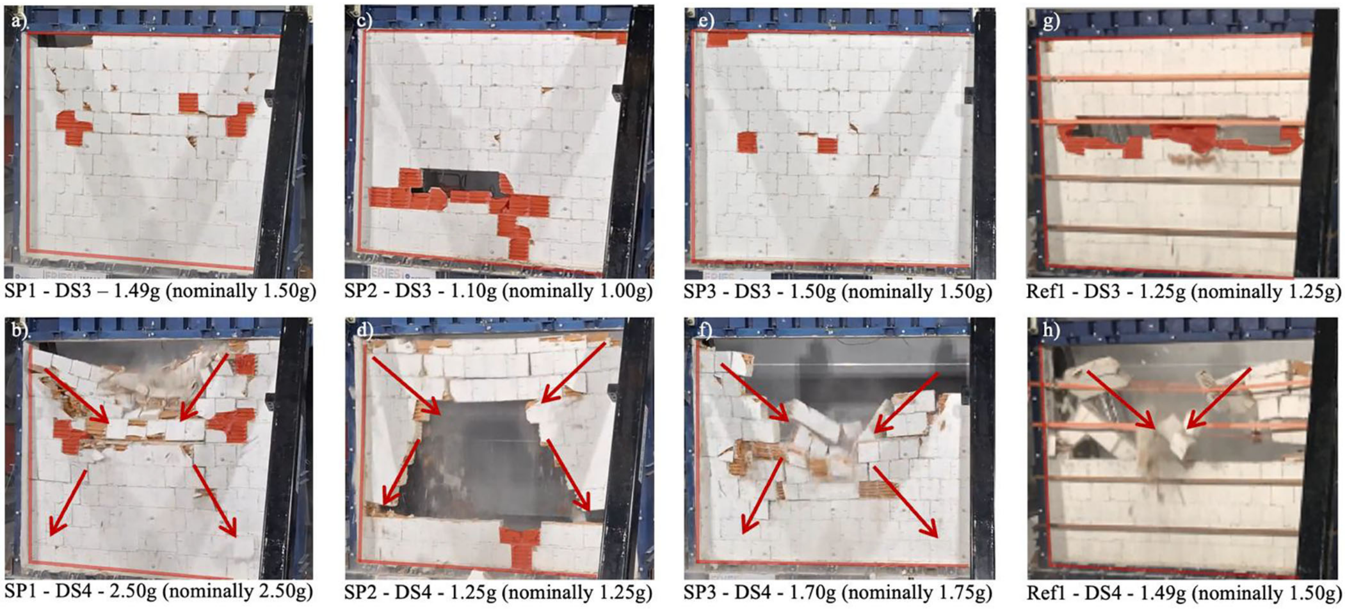

FIGURE 7 | Snapshots of the out-of-plane tests. *Note:* Ref2 is not shown because it sustained a lower maximum in-plane drift than the other specimens; Ref3 was not subjected to an out-of-plane test.

experimental tests and therefore record the corresponding levels of PFA.

3 | Results and Discussion

The results demonstrated that different loading protocols have strongly influenced the specimen responses. This section compares their response in terms of damage evolution, force-displacement response (i.e., hysteretic and envelope/backbone), and energy dissipation.

3.1 | Observed Response

Figure 6 provides a summary of the IP damage observed for specimens SP1, SP2, and SP3, as well as a comparison with the reference tests Ref1 and Ref2 (for which a detailed description is available in Morandi et al., [25]). The figure shows snapshots of the test at the attainment of DS0, DS2, and at the end of the IP phase, also highlighting the cracks that more evidently influenced the overall damage mechanism of the specimens. Damage is shown only considering the plastered side of the infills, since analogous crack patterns were identified on the non-plastered side. Figure 7 shows relevant snapshots of the OOP tests, while the full video recordings are available in the provided data repository.

3.1.1 | Specimen SP1

In specimen SP1, IP damage initiated at 0.05% drift ratio (nominally 0.10%) with the formation of microcracks and partial detachment of the infill from the surrounding frame. As per Table 3, this phenomenon constitutes the attainment of DS0 (Figure 6a). At 0.16% drift (nominally 0.20%), a horizontal crack formed just above mid-height, spanning the middle third of the panel width and propagating along the mortar joint (constituting DS1). As drift increased to 0.26% (nominally 0.30%), the width of this crack increased and diagonal cracks initiated from it, forming a cross-like pattern on both sides of the panel, while still following the mortar layout and not reaching the corners. As per Table 3, this phenomenon constitutes the attainment of DS2 (Figure 6b). At 0.36% drift (nominally 0.40%), diagonal cracks reached the panel corners, and sliding became evident along the main horizontal crack. By 0.47% (nominally 0.50%), two new horizontal cracks developed—one slightly below mid-height and another at three-quarters of the panel height. The presence of more than one major horizontal crack favoured an overall damage mechanism dominated by sliding, at the expense of a diagonal strut-like behaviour. Beyond this point, diagonal cracks mainly formed to ensure displacement compatibility. At 0.63% drift (nominally 0.65%), these additional horizontal cracks widened, while the overall crack pattern stabilised (Figure 6c).

In the OOP phase, SP1 exhibited damage predominantly in the upper portion of the panel throughout the entire loading sequence. No evident damage progression was observed for the 0.15 and 0.28 g PFA runs (nominally 0.10 and 0.20 g). Between 0.39 and 0.59 g (nominally 0.30 and 0.75 g), minor plaster pulverisation was observed. At 1.01 g (nominally 1.00 g), partial clay unit damage started, with the front face of one unit detaching from the infill. Damage worsened between 1.30 and 1.49 g (nominally 1.25 and 1.50 g), where further plaster pulverisation was accompanied by additional external unit face detachment and partial unit damage. At 1.49 g (nominally 1.50 g), the detachment of the infill from the surrounding frame became clearly visible, marking the onset of DS3 (Figure 7a), as defined in Table 3. From 1.78 to 1.98 g (nominally 1.75 and 2.00 g), plaster detachment became more diffuse across the panel surface. At 2.15 g (nominally 2.25 g), heavy plaster damage and detachment concentrated at the top corners. Finally, during the three repeated runs nominally at

2.50 g (measured at 2.33, 2.28, and 2.50 g, respectively), the damage pattern propagated across the panel, leading to the failure and expulsion of the top masonry layer. Collapse (i.e., DS4, Figure 7b) initiated from excessive displacement concentrated over the diagonal cracks in the upper part of the panel. No crushing of the masonry units was observed, and the OOP failure mechanism was governed by snapping.

3.1.2 | Specimen SP2

SP2 exhibited initial microcracking and complete detachment from the frame at 0.06% drift (nominally 0.10%), constituting DS0 (Figure 6d). At 0.14% drift (nominally 0.20%), a horizontal crack initiated at approximately one-third of the panel height, located roughly in the centre of the infill and roughly spanning two masonry units (constituting DS1). This was accompanied by minor sliding. By 0.24% drift (nominally 0.30%), this crack extended to nearly one-third of the panel width, and diagonal cracks emerged on both sides, aligned with vertical mortar joints and spanning five units (constituting DS2, Figure 6e). A second horizontal crack formed at roughly two-thirds of the height on the right side of the panel. At 0.35% drift (nominally 0.40%), crack widths increased, and a third horizontal crack appeared midway between the existing ones. Diagonal cracking continued uniformly across the panel. At 0.46% drift (nominally 0.50%), diffuse cracking became widespread, with plaster spalling along the horizontal and some diagonal cracks. By 0.63% drift (nominally 0.65%), diagonal cracks widened further, developing into a diffuse cracking pattern. Diffused sliding along horizontal cracks increased, leading to breaking and partial expulsion of masonry units. One upper corner showed signs of crushing initiation, accompanied by diffuse and heavy plaster spalling (Figure 6f). Unlike SP1, the damage mechanism in SP2 was dominated by a diagonal strut-like behaviour rather than sliding, confirmed by the diffuse horizontal cracks and the initiation of corner crushing.

In the OOP phase, damage to SP2 was distributed across the entire panel throughout the test. No visible damage progression was evident at 0.17 g PFA (nominally 0.1 g). Minor plaster detachment was visible at 0.30 g (nominally 0.20 g). At 0.40 g (nominally 0.30 g), damage became concentrated in the top left corner, which had already sustained minor crushing during the IP phase. At 0.50 g (nominally 0.40 g), plaster detachment increased, and partial expulsion of unit faces was observed. Detachment of the infill from the surrounding frame started at the top edge, with some damage localised along the horizontal crack in the third masonry layer. No significant change was noted at 0.61 g (nominally 0.50 g), while at 0.85 g (nominally 0.75 g), the top left corner continued to exhibit damage concentration. At this stage, the arch-like resisting system was clearly inactive. At 1.10 g (nominally 1.00 g), several units adjacent to the aforementioned horizontal crack were expelled entirely (Figure 7c), forming a visible hole in the infill (and therefore DS3 according to Table 3). At 1.25 g (nominally 1.25 g), the remaining hanging masonry units began to fail progressively (i.e., DS4, Figure 7d), while the top portion of the infill responded independently until complete collapse occurred. The failure mechanism was governed by snapping, with no sign of crushing of the bricks.

3.1.3 | Specimen SP3

Specimen SP3 initially showed microcracking and partial detachment from the frame at 0.07% drift (nominally 0.10%) - constituting DS0 (Figure 6g)—with the lower left corner remaining attached. At 0.11% drift (nominally 0.15%), a crack formed along this corner. At 0.15% drift (nominally 0.20%), a horizontal crack initiated at approximately three-quarters of the panel height, extending leftward from the centre across two units, while the same crack simultaneously propagated rightward and diagonally (constituting DS1). DS2 was observed at 0.21% drift (nominally 0.25%) when a second diagonal crack formed in the opposite direction, creating a cross pattern (Figure 6h). By 0.25% drift (nominally 0.30%), a horizontal crack developed at mid-height, nearly spanning the entire panel width, accompanied by diffuse cracking mainly along mortar joints. Between 0.31% and 0.41% drift (nominally 0.35% - 0.45%), crack widths progressively increased, with horizontal sliding observed along the mid-height crack and localised plaster spalling. From 0.46% to 0.61% drift (nominally 0.50% - 0.65%), diffuse cracking and spalling continued to increase. At 0.56% (nominally 0.60%), the mechanism was dominated by sliding along the horizontal crack at the centre of the panel, and multiple wedges underwent relative rotations to accommodate the sliding (i.e., displacement compatibility). At 0.61% (nominally 0.65%), masonry unit breakage and partial expulsions were observed. As per SP1, the damage mechanism in SP3 was dominated by a sliding rather than a diagonal strut-like behaviour, confirmed by the fact that there was only one major horizontal crack at mid height (Figure 6i).

As in the case of SP1, specimen SP3 showed OOP damage mainly concentrated in the upper region of the panel throughout the test. At 0.15, 0.28, and 0.40 g PFA (nominally 0.10, 0.20, and 0.30 g), only diffuse and minimal plaster detachment was observed. At 0.52 g (nominally 0.40 g), detachment of the infill from the surrounding frame at the top edge started. No substantial change in damage was recorded at 0.60 g (nominally 0.50 g), except for the expulsion of one unit face.

At 0.86 g (nominally 0.75 g), the damage pattern remained stable, although the larger deformations indicated that the arch-like resisting system was no longer active. At 1.12 g (nominally 1.00 g), plaster detachment became more widespread, with intensified damage at the top corners. At 1.37 g (nominally 1.25 g), significant relative displacement occurred in the top portion of the panel, particularly within the wedge defined by the mid-height horizontal crack, the diagonal cracks, and the top boundary with the frame. This resulted in heavy plaster detachment and widespread unit face expulsion along the same perimeter. At 1.53 g (nominally 1.50 g), the damage pattern exacerbated further (Figure 7e), marking the onset of DS3 (according to Table 3). At 1.70 g (nominally 1.75 g), the infill underwent a complete collapse mechanism (i.e., DS4, Figure 7f) analogous to SP1: the top masonry layer failed and was expelled due to excessive displacement concentrated along the upper diagonal cracks. The failure mechanism was governed by snapping.

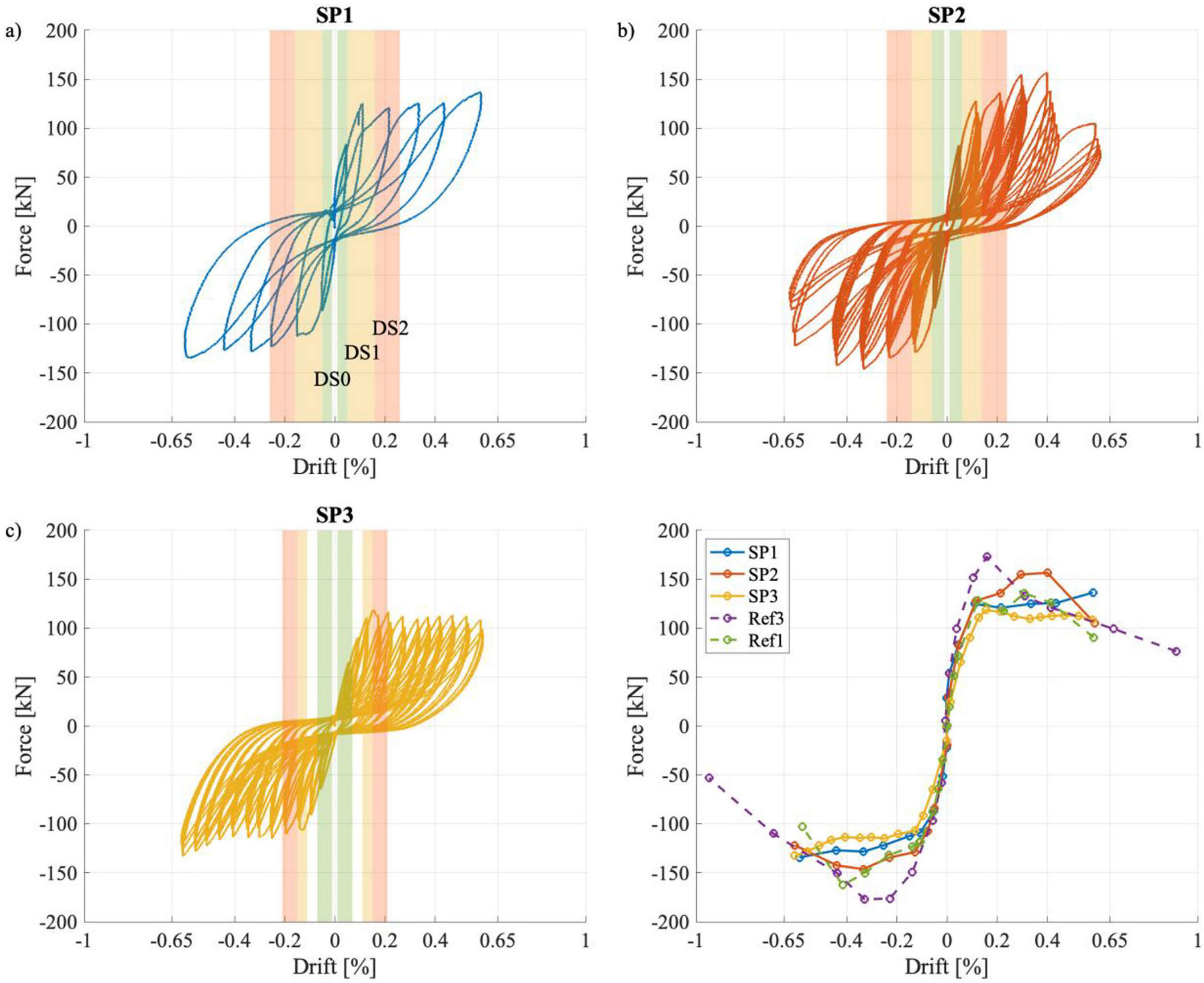

FIGURE 8 | (a–c) In-plane force-displacement response—respectively SP1, SP2, SP3; (d) force-displacement envelopes. *Note:* the force contribution related to the enclosing frame is subtracted to obtain the infill-only response.

3.2 | Measured Response and Test Interpretation

Figure 8a–c shows the measured IP force-displacement responses of the three specimens, also highlighting the drift intervals corresponding to the characterised DS0, DS1, and DS2. The specimens show similar values of the peak force (approximately 150 kN) and imposed peak drift (approximately 0.60%). They show a behaviour sufficiently consistent with the Ref1 and Ref2 specimens in the reference test campaign (Figure 8d), thus confirming the appropriateness of adopting such data for the calibration of the IP protocols. The specimens show notably different shapes of the force-displacement envelopes (Figure 8d). The envelope of specimens SP1 and SP3 is monotonic, with moderate hardening for SP1 while almost no hardening for SP3. Instead, SP2 showed signs of a post-peak behaviour, with the peak presumably located at approximately 0.40% drift. This result is consistent with the observed damage mechanisms of the specimens, with SP1 and SP3 dominated by sliding, and SP2 dominated by a diagonal strut-like behaviour and showing corner crushing. Among other parameters, this difference may be mainly related to the properties of the mortar. The particularly low strength of the mortar, together with the low initial shear strength of the bed joints (Table 1), indicate that a sliding behaviour should be the most likely one. However, the available material data are provided in terms of global statistical values and do not allow for a wall-by-wall characterisation. Moreover, such material properties exhibit a coefficient of variation of 13.8% to 20.3%, indicating a small but non-negligible probability of higher strength values that may prevent sliding-dominated behaviour. At this stage, this interpretation should therefore be regarded as a plausible hypothesis rather than a confirmed explanation, and would require further validation, possibly through a sensitivity analysis based on a calibrated numerical model (micro-modelling approach) exploring different mortar strengths.

Figure 9a–c shows the OOP force-displacement response of the specimens. Displacements are measured at the centre point of the infills (i.e., marker 26, see Figure 2), while the total OOP force is calculated based on the measured accelerations. To do so, each accelerometer is imagined at the centre of a tributary

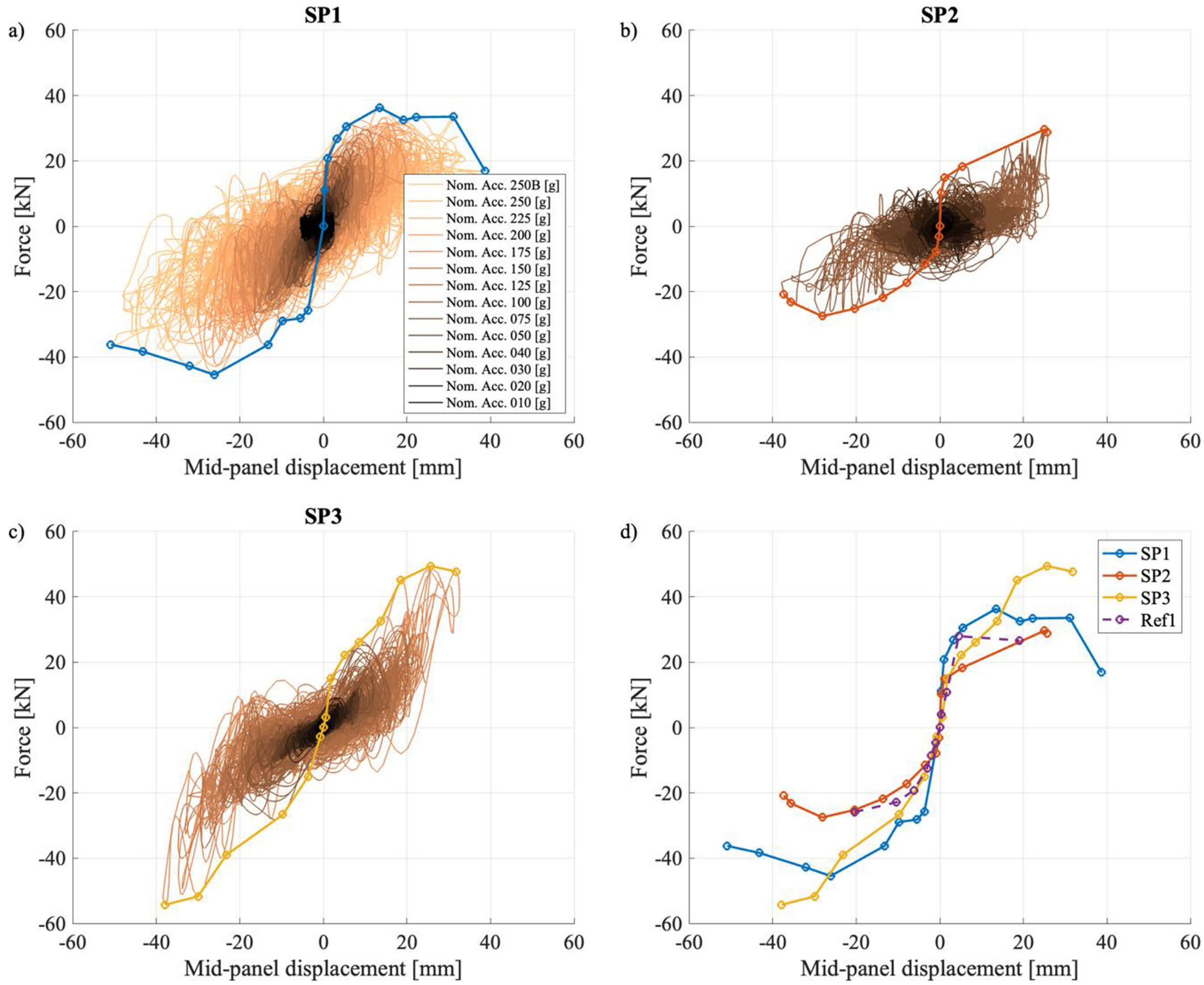

FIGURE 9 | (a–c) Out-of-plane force-displacement response—respectively SP1, SP2, SP3; (d) force-displacement envelopes.

area associated with a corresponding tributary mass (assuming uniform density, see Table 1). Moreover, the acceleration data was resampled applying a linear interpolation in space. Especially in the last test runs, some accelerometers were removed to avoid damaging them. In such cases, linear interpolation/extrapolation was carried out assuming the last available full spatial distribution of accelerations, scaled according to measurement of the central accelerometer (present in all the test runs). Compared to the IP response, the specimens show a relatively larger variability in the peak force (approximately between 25 and 55 kN), which is consistent with the stochastic nature of masonry and correlates directly with the different levels of pre-existing IP damage. Despite these quantitative differences, the qualitative failure mode and the response envelope of the specimens (Figure 9d) remains consistent with the results of specimen Ref1 from the reference test campaign. The force-displacement response is approximately symmetric for all specimens and is characterized by three distinct stages. Initially, a linear response is observed up to the elastic limit. Thereafter, the curves diverge as progressive cracking and localized damage initiate; this stage exhibits a nonlinear response that varies according to each specimen's specific configuration and damage evolution. Finally, after reaching the peak force (observed at approximately 20 mm displacement), the specimens undergo a loss of stability until collapse occurs. This behaviour is consistent with the observed OOP failure mechanism, which is dominated by snapping rather than crushing of the brick. Such mechanism is confirmed by the infill slenderness ratio, which is equal to 2750 mm/120 mm = 22.92. On the other hand, the maximum recorded displacement of the infills is consistent with the level of observed IP damage, and it is approximately equal to 25, 30, and 40 mm for SP2, SP3, and SP1 respectively.

To further summarise the OOP response results, Figure 10 tracks the peak accelerations and deformations of the centre point of the infills (i.e., accelerometer 7 and marker 26, see Figure 2), and a point located at three-quarters of the infills' height along the centre of the panel (i.e., accelerometer 4 and marker 33). Such locations are selected to better grasp the specific OOP failure mechanisms of the different specimens, mainly involving a top wedge for specimens SP1 and SP3 (Figure 7b,f) and the full panel for SP2 (Figure 7d). The results show that the infill response with respect to the peak acceleration measured at the

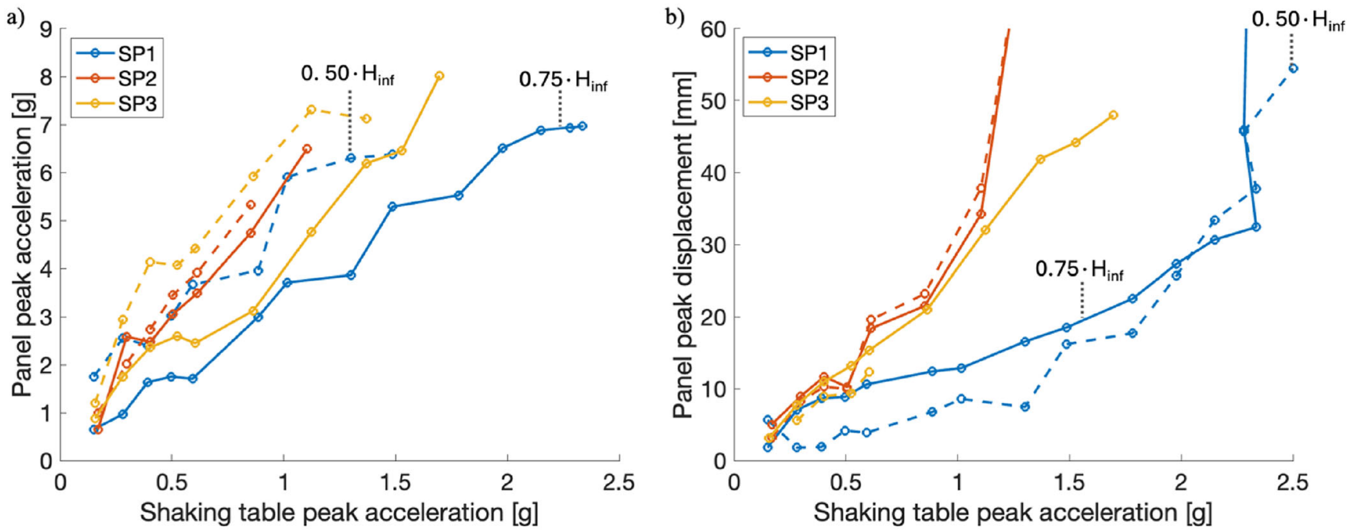

FIGURE 10 | Out-of-plane panel response in terms of acceleration (a) and displacement (b). The line colour indicates the specimen while the line type indicates the position of the measurement along the centre line of the infill, at half and three-quarters of the height (H_{inf}). *Note:* some measurements are missing due to falling plaster hitting the instruments and/or their complete detachment due to the progression of damage; deformations are measured at the step for which the marker at $0.75H_{inf}$ reaches its peak.

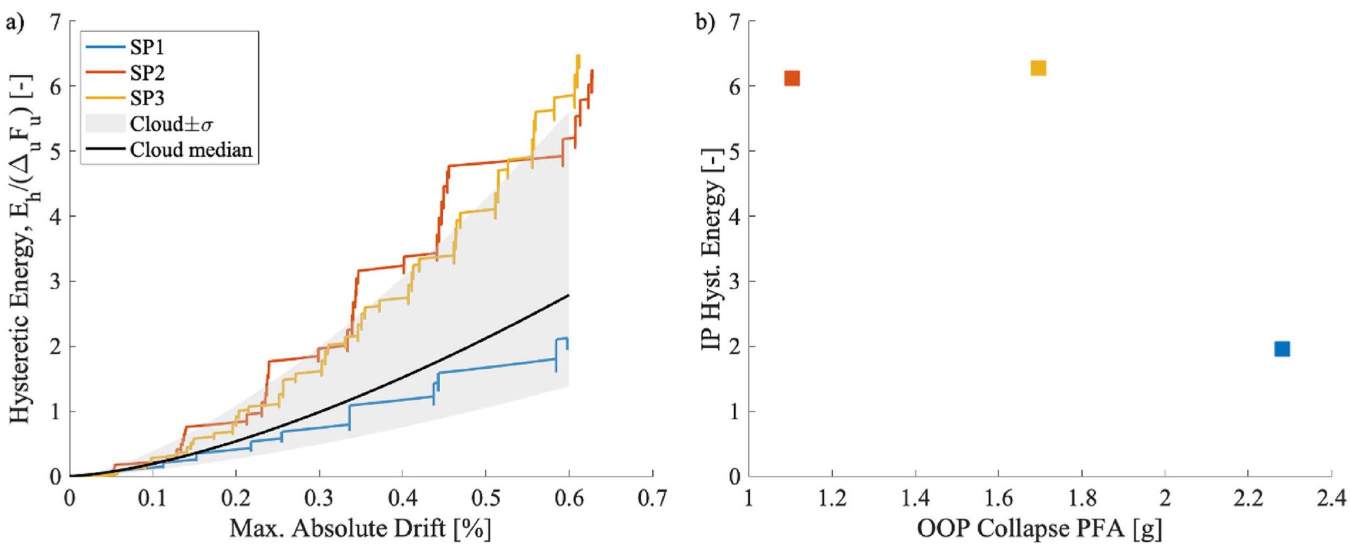

FIGURE 11 | (a) Hysteretic energy versus maximum drift response of the specimens; (b) out-of-plane collapse capacity.

shaking table, both in terms of peak accelerations (Figure 10a) and displacements (Figure 10b) is pseudo-linear until the sudden onset of collapse. This is consistent with the expected OOP behaviour for this kind of element, in which complete collapse is dominated by a sudden global instability following a phase in which only a minor level of damage is observed. This is analogous to the two-way bending mechanism observed in masonry infills, where the multi-linear elastic response with a negative stiffness branch means that the collapse is driven by rigid body mechanics and geometry rather than localised material behaviour [48]. For SP1 and SP3, most of the accelerations concentrated in the upper trapezoidal wedge defined by the IP damage pattern (Section 3.1), as shown by the large differences for the measurements for markers 26 and 33 (Figure 10a). On the other hand, the more distributed IP damage for SP2 implies a more uniform OOP acceleration pattern, with an almost identical measured acceleration for markers 26 and 33. Such behaviour is even more evident when observing the peak displacements, which are almost identical for SP2 but diverge considerably for SP1 and SP3 (for which the marker at three-quarters of the height failed to measure due to extensive damage).

Figure 11a shows the energy-based behaviour of the specimens in the IP phase, while Table 4 quantifies the DSs both in terms of drift and hysteretic energy. The experimental hysteretic energy versus drift relationships of the three specimens closely overlap with the macro-modelling results adopted in the calibration of the IP load protocols (Section 2.6). Specifically, the SP2 and SP3 experimental curves correspond with the estimate one standard deviation above the median obtained with the cloud analysis of

TABLE 4 | Identified IP damage states. Note: The ranges refer to the beginning and the end of a specific IP test phase, assuming that the identified DS may be activated at any point within that specific portion of the test.

Specimen	θ_{DS0}^{obs} [%]	E_{H-DS0}^{obs} [−]	θ_{DS1}^{obs} [%]	E_{H-DS1}^{obs} [−]	θ_{DS2}^{obs} [%]	E_{H-DS2}^{obs} [−]
SP1	0–0.05	0–0.056	0.05–0.16	0.056–0.358	0.16–0.26	0.360–0.689
SP2	0–0.06	0–0.176	0.06–0.14	0.176–0.756	0.14–0.24	0.757–1.765
SP3	0–0.07	0–0.113	0.11–0.15	0.291–0.576	0.15–0.21	0.578–1.012
Ref1	0–0.03	0–0.007	0.03–0.06	0.007–0.096	0.15–0.24	0.431–0.917
Ref3	0–0.02	0–0.006	0.02–0.06	0.006–0.108	0.14–0.24	0.258–0.871

the calibrated macro model. Moreover, the experimental curve for SP1 is slightly above the estimate one standard deviation below the median of the cloud analyses. Such alignment confirms that the mapping of the IP loading parameters and resulting energy dissipation (already studied in the literature) is controllable even with a simplified modelling approach. The results suggest that test campaigns focused on energy quantities may use the first tested specimen to characterise a simplified numerical model, estimate a cloud-based energy-drift relationship, and use the results to design the loading protocols of different specimens.

One result demanding particular attention is the comparison between specimens SP2 and SP3. Those were designed to obtain the same hysteretic energy versus drift relationships, although with a different combination of drift amplitude and cycles. The results show that their energetic behaviour is closely matched, although their damage pattern is notably different (Section 3.1). For specimen SP3, dominated by sliding, energy dissipation was likely correlated to an increase of plastic strains/deformation plasticity (i.e., plasticity), possibly to the detriment of an increase in stiffness/strength deterioration (i.e., damage). The hysteretic energy of SP2, dominated by a strut-like behaviour, likely correlated with an increase of damage rather than plasticity. Such outcome is consistent with the established literature results [49], which identify how hysteretic energy depends on a combination of hysteretic, strength degradation, and damping properties of a system. For realistic structures, such properties in turn depend on material, lateral resisting system, and plastic mechanism. However, numerical studies [15] demonstrated that for masonry-infilled reinforced concrete frames, the IP response mechanism is the most influencing parameter on the hysteretic energy, and therefore, energy can be a sufficient proxy for damage once the governing response mechanism is properly identified. The results of the present campaign confirm this hypothesis: hysteretic energy can be a sufficient proxy for damage levels only after characterising the response mechanism, which is in turn governed by the relative shares of mechanical damage and non-damaging frictional work.

This point is corroborated by using the OOP collapse capacity as a proxy of the influence of hysteretic energy. To do so, Figure 11b shows how the OOP collapse capacity of the specimens varies with the hysteretic energy dissipated throughout the entire IP phase of the tests. To minimise the effect of the different OOP displacement shapes, the OOP collapse capacity was measured with the peak acceleration of the shaking table. It is clear how despite showing a particularly similar IP hysteretic energy, the OOP collapse capacity of specimen SP3 (sliding-dominated) is much larger than the one for SP2 (strut-dominated). The comparison between SP1 and SP3, however, is contingent upon a consistent IP response mechanism (bed-joint sliding). In such case, it is clear how a larger IP hysteretic energy is associated with a lower OOP capacity. Although data was particularly limited and no general conclusion can be drawn yet, it seems that after characterising the dissipative mechanism (and in turn the share of damage and friction-based plasticity), hysteretic energy may explain different damage levels. In future studies, such hypothesis may be tested with a sensitivity analysis (especially varying the mortar characteristics and the IP load parameters) using a refined micro-modelling approach.

4 | Conclusion

This paper presented the research project ENFRAG (ENhancing state-dependent FRAGility through experimentally validated Energy-Based Approaches), part of the ERIES project (Engineering Research Infrastructures for European Synergies). ENFRAG involved experimental tests on three nominally identical masonry infill panels subjected to quasi-static cyclic displacement-controlled IP loads generating a moderate level of damage, followed by dynamic OOP shaking-table testing until collapse. The aim was to study the effect of the IP hysteretic energy dissipation on the observed IP DS, and the subsequent OOP collapse capacity. To do so, different IP loading protocols were designed to induce the same peak amplitude-based EDPs while modulating the energy-based demands. Those were designed by calibrating a numerical model on the results of a previous experimental campaign that adopted the same test setup and four specimens nominally identical to those considered herein. The results are summarised as follows:

1. We proposed a methodology to calibrate numerical model parameters which has not been used before in the context of experimental tests. By maximising the likelihood of a selected numerical model to observe experimental data (i.e., hysteretic energy, in this case), the methodology allows model uncertainty to be calibrated while simultaneously considering multiple experimental test results.
2. We proposed a novel method to define IP loading protocols to explicitly modulate the hysteretic energy versus maximum deformation of a set of specimens. This involves using a simplified modelling strategy (i.e., strut-based macro-modelling, in this case) calibrated based on available test data according to point 1. This was applied to three specimens,

showing a good match between the desired and measured hysteretic energy versus maximum deformation response. The results confirm that the mapping between IP loading parameters and energy dissipation is controllable even with a simplified modelling approach. Therefore, we suggest that test campaigns focused on energy quantities may use the first tested specimen to characterise a simplified numerical model, estimate a cloud-based energy-deformation relationship, and use the results to design the loading protocols for the remaining specimens.

3. The results of the experimental campaign highlight that the IP response mechanism of specimens SP1 and SP3 was dominated by sliding, while that of SP2 was dominated by a diagonal strut-like behaviour. For specimens SP1 and SP3, energy dissipation was likely correlated to an increase of plastic strains/deformation plasticity (i.e., plasticity). The hysteretic energy of SP2 was likely correlated with an increase of damage rather than plasticity. The larger IP hysteretic energy dissipated by SP3 compared to SP1 was associated with a lower OOP capacity. Specimen SP2, which dissipated the same IP energy as SP3 while having a different dissipative mechanism, was associated with a considerably lower OOP capacity.
4. The available experimental data does not constitute a statistically significant sample, and therefore it is not yet possible to fully generalise point 3, since several parameters of the specimens and/or the testing protocols may influence the results. However, a higher strength of the mortar may offer a possible explanation to the transition between a sliding-based and strut-like nonlinear response mechanism. Additional tests should be carried out to verify this outcome. Moreover, such a hypothesis may be tested with a sensitivity analysis using a calibrated numerical model based on a refined micro-modelling approach.
5. As a result of point 3, it seems that hysteretic energy may be a sufficient proxy for damage only when conditioned upon the specific dissipative mechanism of the analysed member/structure (and in turn the share of damage and friction-based plasticity). This result is in line with previous analytical studies on masonry-infilled reinforced concrete frames demonstrating that the nonlinear response mechanism is the most influencing parameter on hysteretic energy. However, it should be noted that the present findings are based on a limited experimental dataset, involving a single typology of brick, mortar, and frame. Therefore, the generalisation of this observation requires further assessment. More extensive experimental tests and/or complementary refined numerical analyses are needed to consolidate these findings. Within these limitations, the results still suggest the potential of using hysteretic energy as a damage proxy within state-dependent seismic fragility assessment methodologies, allowing an explicit consideration of damage accumulation.

Acknowledgments

This study was partially funded by the transnational access project "ERIES–ENFRAG", supported by the Engineering Research Infrastructures for European Synergies (ERIES) project (www.eries.eu), which has received funding from the European Union's Horizon Europe Framework Programme under Grant Agreement No. 101058684. This is ERIES publication number J1. Eng. Soheil Rostamkalaee is gratefully acknowledged for providing processed OOP data.

Data Availability Statement

The data related to the experimental tests conducted within ERIES-ENFRAG are available on the Built Environment Data's Experiments Platform at https://doi.org/10.60756/euc-f8hcyh64, whereas data from the Morandi et al. (2025) campaign also utilised here are available at: https://doi.org/10.60756/euc-uatz37h429

References

1. F. Di Trapani and M. Malavisi, "Seismic Fragility Assessment of Infilled Frames Subject to Mainshock/Aftershock Sequences Using a Double Incremental Dynamic Analysis Approach," *Bulletin of Earthquake Engineering* 17, no. 1 (2019): 211–235, https://doi.org/10.1007/s10518-018-0445-2.

2. A. N. Papadopoulos, M. Kohrangi, and P. Bazzurro, "Mainshock-Consistent Ground Motion Record Selection for Aftershock Sequences," *Earthquake Engineering & Structural Dynamics* no. June 2019 (2020): 754–771, https://doi.org/10.1002/eqe.3263.

3. L. Zhang, K. Goda, F. De Luca, and R. De Risi, "Mainshock-Aftershock State-Dependent Fragility Curves: A Case of Wood-Frame Houses in British Columbia, Canada," *Earthquake Engineering and Structural Dynamics* no. July 2019 (2020): 1–20, https://doi.org/10.1002/eqe.3269.

4. Y. Park and A. H.-S. Ang, "Mechanistic Seismic Damage Model for Reinforced Concrete," *Journal of Structural Engineering* 111, no. 4 (1985): 722–739, https://doi.org/10.1061/(ASCE)0733-9445(1985)111:4(722).

5. A. Teran-Gilmore and J. O. Jirsa, "Energy Demands for Seismic Design Against Low-Cycle Fatigue," *Earthquake Engineering & Structural Dynamics* 36, no. 3 (2007): 383–404, https://doi.org/10.1002/eqe.663.

6. N. Demirbas, C. Durucan, and H. Sahin, "An Energy-Based Method to Calculate the Vulnerability Scores of RC Buildings for Rapid Structural Assessment Methods," *Structures* 41 (2022): 147–158, https://doi.org/10.1016/j.istruc.2022.05.005.

7. C. Shuhaibar, *The Residual Capacity Method: A Damage Model for Reinforced Concrete Structures* (Cornell University, 1995).

8. A. K. Kazantzi and D. Vamvatsikos, "The Hysteretic Energy as a Performance Measure in Analytical Studies," *Earthquake Spectra* 34, no. 2 (2018): 719–739, https://doi.org/10.1193/112816EQS207M.

9. G. W. Housner, "Limit Design of Structures to Resist Earthquakes," in *First World Conference on Earthquake Engineering*, San Francisco, California (1956).

10. Y. H. Chai, "Incorporating Low-Cycle Fatigue Model Into Duration-Dependent Inelastic Design Spectra," *Earthquake Engineering & Structural Dynamics* 34, no. 1 (2005): 83–96, https://doi.org/10.1002/eqe.422.

11. P. K. Malhotra, "Cyclic-Demand Spectrum," *Earthquake Engineering & Structural Dynamics* 31, no. 7 (2002): 1441–1457, https://doi.org/10.1002/eqe.171.

12. S. K. Kunnath and Y. H. Chai, "Cumulative Damage-Based Inelastic Cyclic Demand Spectrum," *Earthquake Engineering & Structural Dynamics* 33, no. 4 (2004): 499–520, https://doi.org/10.1002/eqe.363.

13. P. Fajfar, "Equivalent Ductility Factors, Taking Into Account Low-Cycle Fatigue," *Earthquake Engineering & Structural Dynamics* 21, no. 10 (1992): 837–848, https://doi.org/10.1002/eqe.4290211001.

14. C.-M. Uang and V. V. Bertero, "Evaluation of Seismic Energy in Structures," *Earthquake Engineering & Structural Dynamics* 19, no. 1 (1990): 77–90, https://doi.org/10.1002/eqe.4290190108.

15. R. Gentile and C. Galasso, "Hysteretic Energy-Based state-Dependent Fragility for Ground-Motion Sequences," *Earthquake Engineering &*

Structural Dynamics 50, no. 4 (2021): 1187–1203, https://doi.org/10.1002/eqe.3387.

16. L. D. Decanini, F. Mollaioli, and R. Saragoni, "Energy and Displacement Demands Imposed by Near-Source Ground Motions," in *12th World Conference on Earthquake Engineering*, Auckland, New Zealand (2000).

17. G. A. Tropea, G. Angelucci, D. Bernardini, G. Quaranta, and F. Mollaioli, "An Energy Based Method to Evaluate Reinforced Concrete Column Seismic Capacity," *Structures* 78 (2025): 109276, https://doi.org/10.1016/j.istruc.2025.109276.

18. G. A. Tropea, G. Angelucci, D. Bernardini, G. Quaranta, and F. Mollaioli, "New Energy-Based Methodology to Characterize Nonlinear Seismic Response," *Engineering Structures* 325 (2025): 119488, https://doi.org/10.1016/j.engstruct.2024.119488.

19. P. Ricci, M. Di Domenico, and G. M. Verderame, "Empirical-Based Out-of-Plane URM Infill Wall Model Accounting for the Interaction With In-Plane Demand," *Earthquake Engineering & Structural Dynamics* 47, no. 3 (2018): 802–827, https://doi.org/10.1002/eqe.2992.

20. P. Morandi, S. Hak, R. R. Milanesi, and G. Magenes, "In-Plane/Out-of-Plane Interaction of Strong Masonry Infills: From Cyclic Tests to Out-of-Plane Verifications," *Earthquake Engineering & Structural Dynamics* 51, no. 3 (2022): 648–672, https://doi.org/10.1002/eqe.3584.

21. R. R. Milanesi, P. Morandi, C. F. Manzini, L. Albanesi, and G. Magenes, "Out-of-Plane Response of an Innovative Masonry Infill With Sliding Joints From Shaking Table Tests," *Journal of Earthquake Engineering* 26, no. 4 (2022): 1789–1823, https://doi.org/10.1080/13632469.2020.1739173.

22. A. Furtado, H. Rodrigues, A. Arede, and H. Varum, "Experimental Investigation on the Possible Effect of Previous Damage, Workmanship and Test Setup on the Out-of-Plane Behaviour of Masonry Infill Walls," *Journal of Earthquake Engineering* 26, no. 11 (2022): 5647–5678, https://doi.org/10.1080/13632469.2021.1882359.

23. A. Milijaš, M. Marinković, C. Butenweg, and S. Klinkel, "Experimental Results of Reinforced Concrete Frames With Masonry Infills With and Without Openings Under Combined Quasi-Static In-Plane and Out-of-Plane Seismic Loading," *Bulletin of Earthquake Engineering* 21, no. 7 (2023): 3537–3579, https://doi.org/10.1007/s10518-023-01664-4.

24. F. Gutiérrez-Urzúa, F. Freddi, and E. Tubaldi, "Seismic Risk and Failure Modes Assessment of Steel BRB Frames Under Earthquake Sequences," *Structural Safety* 115 (2025): 102598, https://doi.org/10.1016/j.strusafe.2025.102598.

25. P. Morandi, M. Kurukulasuriya, R. R. Milanesi, et al., "Dynamic Shaking Table Out-of-Plane Tests on Weak Masonry Infills With and Without Previous In-Plane Loading," *Journal of Building Engineering* 100 (2025): 111670, https://doi.org/10.1016/j.jobe.2024.111670.

26. EN 772-1. Methods of Test for Masonry Units—Determination of Compressive Strength. Brussels, Belgium: 2015.

27. EN 1015-11. Methods of Test for Mortar for Masonry—Determination of Flexural and Compressive Strength of Hardened Mortar. Brussels, Belgium: 2019.

28. EN 1052-1. Methods of Test for Masonry—Determination of Compressive Strength. Brussels, Belgium: 2001.

29. ASTM E519-02. Test Method for Diagonal Tension (Shear) in Masonry Assemblages (ASTM International, 2002).

30. EN 1052-2. Methods of Test for Masonry—Determination of Flexural Strength. Brussels, Belgium: 2007.

31. EN 1052–3. Methods of Test for Masonry—Determination of Initial Shear Strength. Brussels, Belgium: 2007.

32. D. Bolognini and F. Dacarro, "Prove Di Qualifica Sismica Su Tavola Vibrante di Trasformatori di Tensione (in Italian)," *Progettazione Sismica* 10, no. 2 (2018): 49–60, https://doi.org/10.7414/PS.10.2.49-60.

33. ICC-ES AC156. Acceptance Criteria for Seismic Qualification by Shake Tale Testing of Non-Structural Components and Systems. 2000.

34. B. Stafford Smith, "Methods for Predicting the Lateral Stiffness and Strength of Multi-Storey Infilled Frames," *Building Science* 2, no. 3 (1967): 247–257, https://doi.org/10.1016/0007-3628(67)90027-8.

35. F. McKenna, G. L. Fenves, and M. H. Scott, (2000), *Open System for Earthquake Engineering Simulation*.

36. L. Liberatore, F. Noto, F. Mollaioli, and P. Franchin, "In-Plane Response of Masonry Infill Walls: Comprehensive Experimentally-Based Equivalent Strut Model for Deterministic and Probabilistic Analysis," *Engineering Structures* 167 (2018): 533–548, https://doi.org/10.1016/j.engstruct.2018.04.057.

37. P. Gardoni, A. Der Kiureghian, and K. M. Mosalam, "Probabilistic Capacity Models and Fragility Estimates for Reinforced Concrete Columns Based on Experimental Observations," *Journal of Engineering Mechanics* 128, no. 10 (2002): 1024–1038, https://doi.org/10.1061/(ASCE)0733-9399(2002)128:10(1024).

38. D. E. Goldberg and J. H. Holland, "Genetic Algorithms and Machine Learning," *Machine learning* 3, no. 2–3 (1988): 95–99, https://doi.org/10.1023/A:1022602019183.

39. C. Baggio, A. V. Pinto, and F. Taucer, (2007), Field Manual for Post-Earthquake Damage and Safety Assessment and Short Term Countermeasures (AeDES).

40. D. Cardone and G. Perrone, "Developing Fragility Curves and Loss Functions for Masonry Infill Walls," *Earthquakes and Structures* 1 (2015): 257–279, https://doi.org/10.12989/eas.2015.9.1.257.

41. K. Sassun, T. J. Sullivan, P. Morandi, and D. Cardone, "Characterising the In-Plane Seismic Performance of Infill Masonry," *Bulletin of the New Zealand Society for Earthquake Engineering* 49, no. 1 (2016): 98–115, https://doi.org/10.5459/bnzsee.49.1.98-115.

42. A. Chiozzi and E. Miranda, "Fragility Functions for Masonry Infill Walls With in-Plane Loading," *Earthquake Engineering & Structural Dynamics* 46, no. 15 (2017): 2831–2850, https://doi.org/10.1002/eqe.2934.

43. P. Morandi, S. Hak, and G. Magenes, "Performance-Based Interpretation of In-Plane Cyclic Tests on RC Frames With Strong Masonry Infills," *Engineering Structures* 156 (2018): 503–521, https://doi.org/10.1016/j.engstruct.2017.11.058.

44. European Committee for Standardisation (CEN). EN 1998-1. Eurocode 8: Design of *Structures* for *Earthquake Resistance*. Part 1: General *Rules*, Seismic *Action* and *Rules* for *Buildings*. Brussels, Belgium: 2005.

45. M. T. De Risi, C. Del Gaudio, P. Ricci, and G. M. Verderame, "In-Plane Behaviour and Damage Assessment of Masonry Infills With Hollow Clay Bricks in RC Frames," *Engineering Structures* 168 (2018): 257–275, https://doi.org/10.1016/j.engstruct.2018.04.065.

46. M. Di Domenico, P. Ricci, and G. M. Verderame, "Experimental Assessment of the Out-of-Plane Strength of URM Infill Walls With Different Slenderness and Boundary Conditions," *Bulletin of Earthquake Engineering* 17, no. 7 (2019): 3959–3993, https://doi.org/10.1007/s10518-019-00604-5.

47. B. Pradhan, M. Zizzo, V. Sarhosis, and L. Cavaleri, "Out-of-Plane Behaviour of Unreinforced Masonry Infill Walls: Review of the Experimental Studies and Analysis of the Influencing Parameters," *Structures* 33 (2021): 4387–4406, https://doi.org/10.1016/j.istruc.2021.07.038.

48. A. Furtado, H. Rodrigues, and A. Arêde, "Damage Index Model for Masonry Infill Walls Subjected to Out-of-Plane Loadings," in *Energy-Based Seismic Engineering. IWEBSE 2023*, Lecture Notes in Civil Engineering, ed. H. Varum, A. Benavent-Climent, and F. Mollaioli, (Springer, 2023), https://doi.org/10.1007/978-3-031-36562-1_21.

49. U. Tomassetti, F. Graziotti, A. Penna, and G. Magenes, "Modelling One-Way Out-of-Plane Response of Single-Leaf and Cavity Walls," *Engineering Structures* 167 (2018): 241–255, https://doi.org/10.1016/j.engstruct.2018.04.007.